December 2001

Deformation-Enhanced Fluctuations in the Red Cell Skeleton with Theoretical Relations to Elasticity, Connectivity, and Spectrin Unfolding

James C-M. Lee
University of Pennsylvania

Dennis E. Discher
University of Pennsylvania, discher@seas.upenn.edu

Reprinted from *Biophysical Journal*, Volume 81, Issue 6, December 2001, pages 3178-3192.
Publisher URL: http://www.biophysj.org/cgi/reprint/81/6/3178

Deformation-Enhanced Fluctuations in the Red Cell Skeleton with Theoretical Relations to Elasticity, Connectivity, and Spectrin Unfolding

Abstract

To assess local elasticity in the red cell's spectrin-actin network, nano-particles were tethered to actin nodes and their constrained thermal motions were tracked. Cells were both immobilized and controllably deformed by aspiration into a micropipette. Since the network is well-appreciated as soft, thermal fluctuations even in an unstressed portion of network were expected to be many tens of nanometers based on simple equipartition ideas. Real-time particle tracking indeed reveals such root-mean-squared motions for 40-nm fluorescent beads either tethered to actin directly within a cell ghost or connected to actin from outside a cell via glycophorin. Moreover, the elastically constrained displacements are significant on the scale of the network's internodal distance of ~60-80 nm. Surprisingly, along the aspirated projection—where the network is axially extended by as much as twofold or more—fluctuations in the axial direction are *increased* by almost twofold relative to motions in the unstressed network. The molecular basis for such strain softening is discussed broadly in terms of force-driven transitions. Specific considerations are given to 1) protein dissociations that reduce network connectivity, and 2) unfolding kinetics of a localized few of the red cell's ~10^7 spectrin repeats.

Comments

Reprinted from *Biophysical Journal*, Volume 81, Issue 6, December 2001, pages 3178-3192.
Publisher URL: http://www.biophysj.org/cgi/reprint/81/6/3178

Deformation-Enhanced Fluctuations in the Red Cell Skeleton with Theoretical Relations to Elasticity, Connectivity, and Spectrin Unfolding

James C-M. Lee and Dennis E. Discher
School of Engineering and Applied Science, and Structural Biology Program–The Wistar Institute, University of Pennsylvania, Philadelphia, Pennsylvania 19104 USA

ABSTRACT To assess local elasticity in the red cell's spectrin-actin network, nano-particles were tethered to actin nodes and their constrained thermal motions were tracked. Cells were both immobilized and controllably deformed by aspiration into a micropipette. Since the network is well-appreciated as soft, thermal fluctuations even in an unstressed portion of network were expected to be many tens of nanometers based on simple equipartition ideas. Real-time particle tracking indeed reveals such root-mean-squared motions for 40-nm fluorescent beads either tethered to actin directly within a cell ghost or connected to actin from outside a cell via glycophorin. Moreover, the elastically constrained displacements are significant on the scale of the network's internodal distance of ~60-80 nm. Surprisingly, along the aspirated projection—where the network is axially extended by as much as twofold or more—fluctuations in the axial direction are *increased* by almost twofold relative to motions in the unstressed network. The molecular basis for such strain softening is discussed broadly in terms of force-driven transitions. Specific considerations are given to 1) protein dissociations that reduce network connectivity, and 2) unfolding kinetics of a localized few of the red cell's $\sim 10^7$ spectrin repeats.

INTRODUCTION

When a simple linear chain—in a network or not (Discher et al., 1998)—is stretched to a length comparable to its contour, it generally exhibits a nonlinear stiffening response as thermal fluctuations are suppressed. A multidomain protein such as spectrin, in contrast, can be "over"-stretched through domain unfolding, at least at the single molecule level in vitro (Rief et al., 1998; Lenne et al., 2000; Carl et al., manuscript in preparation). As a result of such transitions, the stress response of the chain or network can be effectively softened. Perhaps suggestive of such a process or other semi-reversible disruptions in the red cell's spectrin-actin network was an early report of progressive force relaxation during micropipette aspiration (Markle et al., 1983). The network has also been shown to soften with increasing temperature T, i.e., the shear modulus $\mu(T)$ decreases (Waugh and Evans, 1979), appearing at odds with the simplest entropic elasticity models ($\mu \approx k_BT \times$ crosslink density) that otherwise provide first estimates for $\mu \sim 0.001$-0.01 pN/nm (Evans and Skalak, 1980; Discher et al., 1998). Whether spectrin unfolding or other mechanisms of network softening occur, for example, in hyperextended regions of the spectrin-actin network in situ is among currently unanswered questions. Toward addressing this, we present a nano-resolution bead-tracking approach to probe local elasticity through thermal fluctuations in the intact network.

Received for publication 5 March 2001 and in final form 24 September 2001.

Address reprint requests to Dr. Dennis Discher, Biophysical Engineering Lab, University of Pennsylvania, 112 Towne Bldg., Philadelphia, PA 19104-6315. Tel.: 215-898-4809; Fax: 215-573-6334; E-mail: discher@seas.upenn.edu.

0006-3495/01/12/3178/15 $2.00

Motivation for understanding the nanoscale motions of the network is further found in the influence that it has on the dynamic organization of other important membrane components. A number of proteins that contribute to the red cell glycocalyx, such as the GPI-linked protein CD-59, are certainly mobile on the cell surface, and have only fleeting steric interactions with network-linked components (Discher et al., 1994). However, the network-linked components that include glycophorins and much of band 3 are often described as predominantly "immobile," based on micron-resolution methodologies that utilize fluorescence and/or photobleaching (e.g., Golan and Veatch, 1980; Discher et al., 1994). The nanoscale mobility that these linked components truly possess, in defining a time-averaged radius of gyration, no doubt underlies glycocalyx function on time scales important to, for instance, intercellular adhesion or its inhibition.

To address issues of constrained mobility, elasticity, and strain-softening or stiffening, we have measured the thermal-average displacements, $\langle \vec{u} \rangle$, of network-linked beads in the plane of the membrane (Fig. 1). Collective bending undulations of the membrane are suppressed through tensions imposed by aspirating a cell or resealed ghost into a micropipette. The micropipette also enables examination of thermal motions in both unstrained or highly extended regions of the network. Wherever the bead, its fluctuations are both driven by k_BT (=4.1 pN nm) and constrained by network elasticity (e.g., Chaikin and Lubensky, 1995). In the equilibrated state, $\langle \vec{u} \rangle$ should thus vanish, but the mean-squared displacements, $\langle \vec{u}^2 \rangle$, should prove non-zero. Relatively recent microrheology methods exploit the equipartition principle—where k_BT drives each mode—through a generalization to viscoelastic materials including gels and cytoskeletal networks. The methods have typically quantified the fluctuations of micron-diameter colloids either embedded in (Gittes et al., 1997; Yamada et al., 2000) or directly bound (McGrath et al., 2000) to a probed

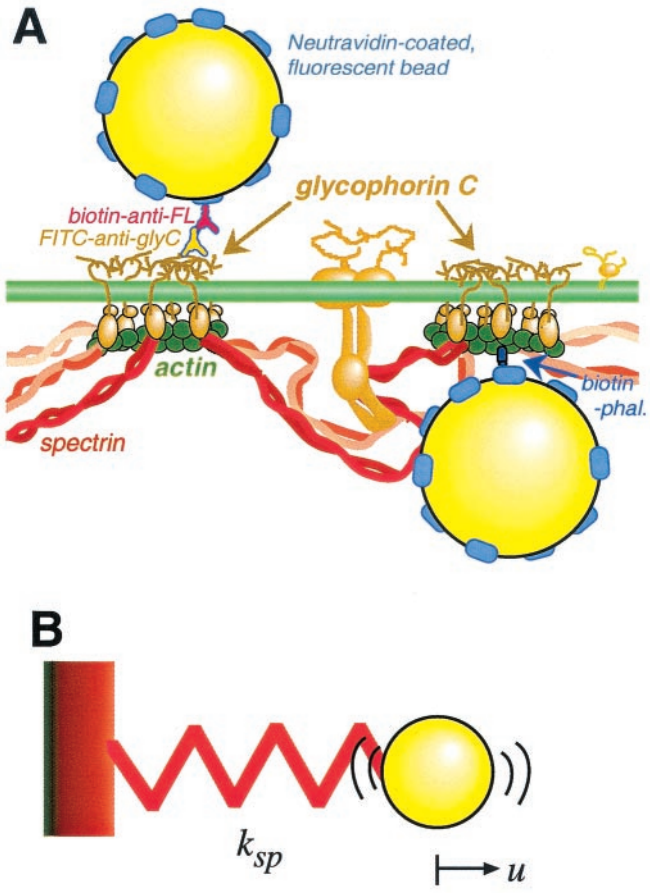

FIGURE 1 Scaled schematic of nano-particle attachments to the red cell membrane. (*A*) In one approach, a neutravidin-coated, red fluorescent bead is bound to the extracellular domain of glycophorin C through FITC-anti-glyC coupled to biotin-anti-FL. In a second approach, a neutravidin-coated, red fluorescent bead inside a ghosted cell is bound to skeletal F-actin protofilaments through biotin-phalloidin. Both beads are ~40 nm in diameter, which is approximately the same length as the 35-nm-long actin protofilaments (Byers and Branton, 1985; Shen et al., 1986; Ursitti and Fowler, 1994) that lie tangent to the bilayer (Picart and Discher, 1999; Picart et al., 2000). The spectrin-actin nodes attach to the lipid bilayer via protein 4.1-mediated interactions with glycophorin C (Chasis and Mohandas, 1992). (*B*) The network acts as an effective spring that constrains the thermal motions of network-attached beads.

material. The erythrocyte membrane, being two-dimensional, allows no choice but to biochemically attach molecule-tracking beads, while the softness of the network, as pointed out from simulation (Discher et al., 1998), should make root-mean-squared (r.m.s.) fluctuations more than large enough to be measured by nanometer-resolution video particle-tracking (Sheetz et al., 1989; Hicks and Angelides, 1995; Tomishige and Kusumi, 1999).

METHODS

Nanometer-resolution fluorescent multiparticle tracking system

An intensified CCD camera (Hamamatsu #500) is used for video imaging of particles through an oil immersion 60×, 1.4 NA objective on a Nikon TE-300 microscope. The highly magnified image is directly fed to a high throughput frame-grabber (National Instruments 1400, Austin, TX) in a 200 MHz PC. Custom software written for IMAQ-LabView (National Instruments) identifies the particle centroids through either a real-time binary mask weighting scheme or a post-experiment Gaussian fit of particle image intensities. The x_i coordinates ($i = 1, 2$) at each 33.3-ms interval were stored in an accessible spreadsheet. Table 1 shows that the percentage difference between the two methods, involving real-time or off-line analysis, is <3% for various experimental setups.

TABLE 1 Direction-averaged root-mean-squared displacements, $\overline{\sqrt{\langle u^2 \rangle}}$, of beads determined by both real-time binary-mask and Gaussian-fit algorithms

Experiment	$\overline{\sqrt{\langle u^2 \rangle}}$ (nm)	% Difference between Tracking Methods
Immobilized beads on coverslip (10 beads)	6.1	2.6
Immobilized beads on micropipette (12 beads)	7.4	1.4

Particle tracking and mechanical stability of the apparatus

Tracking experiments were performed simultaneously with holding a red cell or ghost "stationary" in a micropipette that was cantilevered into a water-filled microscopy chamber. While minimizing possible artifacts that could arise from either cell adhesion to a coverslip or convection currents in the chamber, the use of a holding micropipette required a zero-point motion calibration before each experiment: a 40-nm fluorescent bead on the micropipette was tracked (Fig. 2). Centroidal fluctuations (SD) generally ranged from 5 to 8 nm (e.g., Table 1); similar zero-point stability in related particle-tracking systems has been reported by others (Hicks and Angelides, 1995; Simson et al., 1998).

Fluorescent beads affixed to glycophorin C

Neutravidin-coated 40-nm red fluorescent beads (Molecular Probes, Eugene, OR) were prepared for specific labeling to cells by suspending beads (2 μl, 5.7×10^{14} beads/ml) in phosphate-buffered saline (PBS) (10 μl) that contained bovine serum albumin (BSA) (30 mg/ml) plus dextran (20 mg/ml) and biotin (2 μg/ml). The BSA and dextran were added to suppress nonspecific binding, and biotin was added to titrate the neutravidin binding sites down to just a few per bead.

Bead labeling of the extracellular domain of glycophorin C was achieved through a chain of two antibodies: fluorescein isothiocyanate-labeled anti-glycophorin C (FITC-anti-glyC) (International Blood Group Reference Laboratory, Bristol, UK) was coupled to biotinylated-anti-fluorescein (biotin-anti-FL) (Molecular Probes) as illustrated schematically in Fig. 1 *A*. Packed red cells (5 μl) were first suspended in PBS (15 μl), and FITC-anti-glyC was added (up to 0.02 μg/ml). Labeling was verified by fluorescence microscopy at this stage or later. After 5 min, excess FITC-anti-glyC was removed with the supernatant after centrifugation. Labeled cells were resuspended in PBS (15 μl), and biotin-anti-FL was added (3 μg/ml) for a short incubation (5 min). Beads were subsequently added (1×10^{10} beads/ml) and, after 5 min, the suspension was centrifuged (1200 × *g*) to remove excess beads with the supernatant. Specificity of bead-labeling was demonstrated by quantifying the number of beads bound per cell membrane at several concentrations of both antibodies used. As shown in Fig. 3 *A*, only a few beads bound to glycophorin C and in approximately logarithmic proportion to low concentrations of FITC-anti-glyC under a comparative excess of biotin-anti-FL. Without biotin-anti-FL, no beads

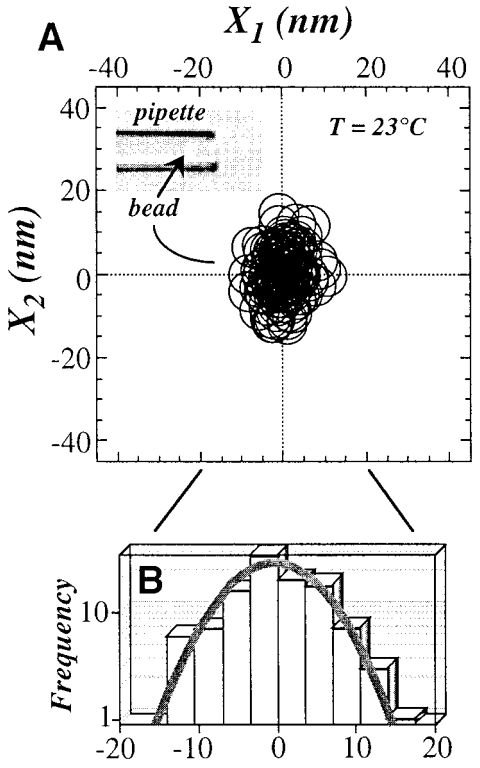

FIGURE 2 The centroid of a 40-nm fluorescent bead adsorbed onto a micropipette was tracked (see Methods) for >4 s and is shown as both a scatterplot (*A*) and as a distribution projected onto the x_1-axis (*B*). The inset shows a superposition of fluorescence and bright-field images. The scatterplot shows that no datapoints—depicted as circles of radius set by the root-mean-squared (r.m.s.) displacement of ~5 nm—are >15 nm away from the origin. Consistent with random noise, the parabolic fit of the measurement frequency on a logarithmic scale shows the reasonableness of a Gaussian fit to the data. Comparable fits were found in both the *1*- and *2*-directions, suggesting that the pipette glass introduces little to no optical distortion.

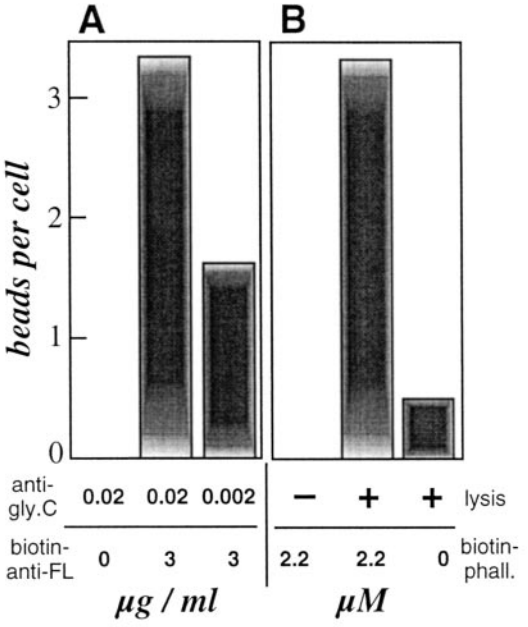

FIGURE 3 Specificity of methods for membrane labeling with neutravidin-covered beads. (*A*) Bead binding to glycophorin C was verified by varying the concentration of either FITC-anti-glyC or biotin-anti-FL. Cell concentration was 30% by volume of packed cells. (*B*) Bead binding to F-actin was effected during hypotonic lysis of cells in which small probes, either beads or biotin-phalloidin, can diffuse in. Biotin phalloidin is a well-known ligand for F-actin. Beads were added to packed cells (30% by volume). Nonspecific binding is ~10% or less of specific binding. In all labeling procedures, beads were precoated with dextran and BSA to suppress the nonspecific binding.

bound to the cell membranes. Tracking experiments were generally done in diluted PBS (~200-270 mOsm).

Fluorescent beads affixed to cytoskeletal F-actin

Beads were also bound to actin protofilaments inside cell ghosts (Fig. 1 *A*). Red cells were reversibly permeabilized by cold, hypotonic lysis, allowing biotin-phalloidin in the lysis buffer to diffuse into the permeabilized cell and bind (Takakuwa et al., 1986; Lieber and Steck, 1989; Discher et al., 1995). Labeling of cytoskeletal actin with fluorescent phalloidins has been described previously (e.g., Discher et al., 1995). Open cell ghosts were washed three times (centrifuging at 1200 × *g*) to remove excess biotin-phalloidin; and packed; labeled membranes were then resuspended (15 μl) in cold lysis buffer (10 mM phosphate, pH 7.4) containing a trace amount of the bead suspension (<0.5 μl, giving 2×10^{11} beads/ml). After 5 min, ghosts were resealed with 100 mM KCl and 1 mM $MgCl_2$ by warming at 37°C for 20-60 min. Bead-labeled ghosts were finally sedimented by centrifugation (1200 × *g*) and excess beads in the supernatant were removed; experiments were done in diluted PBS (~200 mOsm). Specificity of beads attaching to F-actin via biotin was demonstrated by either varying the concentration of biotin-phalloidin or omitting permeabilization. In the absence of biotin-phalloidin, nonspecific binding was found to be ~10% of specific binding (Fig. 3 *B*); nonspecific binding was probably due in part to beads being trapped inside the cell ghost after membrane resealing. When cells were not lysed, no beads bound to the cells even with biotin-phalloidin in the buffer. To suppress nonspecific binding, dextran and BSA were added to all labeling buffers. To reduce crosslinking, neutravidin-coated beads were preincubated with appropriate amounts of biotin.

RESULTS

Thermal motions of F-actin and glycophorin C in unstrained regions of network

A typical particle tracking experiment was begun by pulling a bead-labeled cell into a micropipette. The cell was then slowly aspirated in-and-out to position the bead near the center of the spherical contour of membrane external to the pipette (Fig. 4 *A*). In this central location the bead fluctuates on an essentially flat surface, with relevant geometric corrections being well below measurement noise. Importantly, in-plane strains in this outer region of the deformed network are also known to be extremely small (Discher et al., 1998), even though bending undulations of the membrane are largely suppressed (Evans and Rawicz, 1990) by the aspiration-imposed bilayer tension of ~1 mN/m.

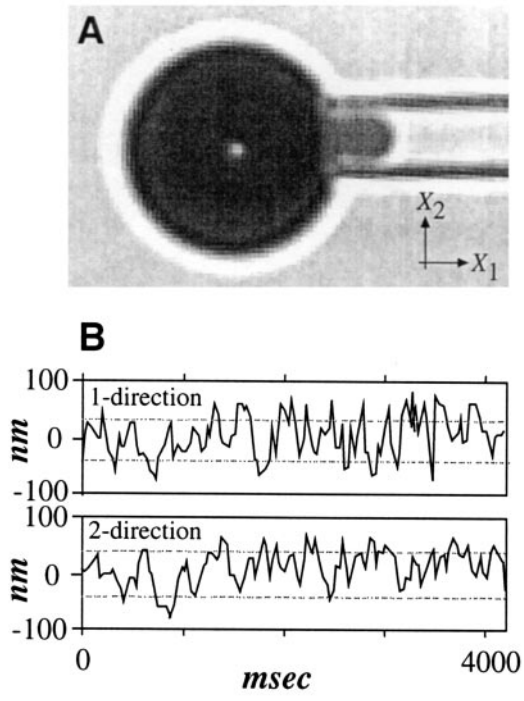

FIGURE 4 Nanoparticle tracking. (*A*) Superposition of cell (bright field) and bead (fluorescent) images showing the position of a single bead on the aspirated cell surface. The swollen cell was immobilized with a micropipette. (*B*) Constrained displacements of the bead over time. The fluctuation amplitude is seen to be a significant fraction of the network's internodal distance, which transmission electron microscopy (TEM) (e.g., Byers and Branton, 1985) and atomic force microscopy (AFM) (Takeuchi et al., 1998) have suggested to be $\xi \approx$ 60-80 nm (Byers and Branton, 1985). Tracking was done only when the bead was centrally located in the outer spherical contour.

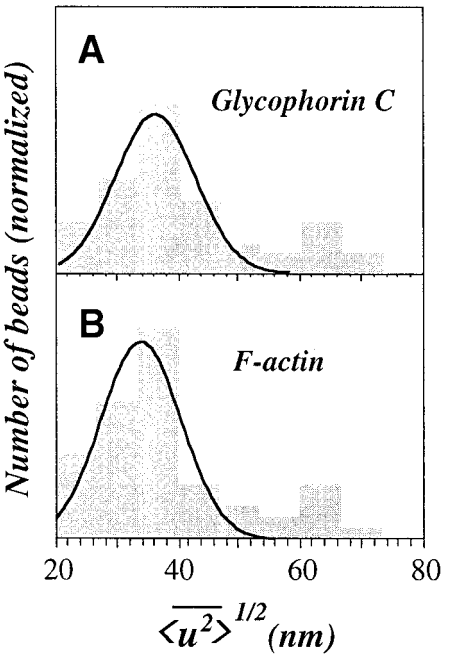

FIGURE 5 The r.m.s. displacements of beads located on the outer spherical contour of aspirated cells. Beads were attached to either (*A*) F-actin or (*B*) glycophorin C and results for >50 cells are cumulated. More than 90% of both datasets show r.m.s. fluctuations <54 nm. The beads giving these results are considered to be specifically bound in the sense of Fig. 3 and are, therefore, fit to Gaussians with respective means (±SD) of 34 ± 6.6 nm and 36 ± 6.6 nm for F-actin and glycophorin C.

In each of the two x_i directions beads on both F-actin and glycophorin C exhibit nanoscale displacements consistent with a solid-like network. Presumably due to the tight interconnections between molecules, bead trajectories scale trivially with time, t, for 10 s or more of tracking (i.e., $x_i \sim t^{\alpha=0}$) as opposed to exhibiting, for example, simple diffusion for which $\alpha = 0.5$. Over a given time interval (typically 10 s), $\langle x_i \rangle$ is well-defined and allows determination of the relative bead displacement as $u_i = x_i - \langle x_i \rangle$. Although $\langle u_i \rangle = 0$, bead fluctuations about this average origin are not suppressed because the network is soft (Fig. 4 *B*): $\langle u_i^2 \rangle = \langle x_i^2 \rangle - \langle x_i \rangle^2 \neq 0$. Root-mean-square displacements, $\sqrt{\langle u_i^2 \rangle}$, were direction-averaged by summing over $i = 1$, 2 and dividing by two, giving $\sqrt{\langle u^2 \rangle}$. Beads tethered to either glycophorin C or F-actin show nearly identical distributions for this mean (Fig. 5) with >90% of the data in a peak centered at 30-40 nm; a second small peak at higher values could reflect artifacts in labeling or instrument noise. Gaussian fits made to the major peaks yield mean values of $\sqrt{\langle u^2 \rangle} = 34$-36 nm (Table 2). Based on both near-identical averages and near-identical standard deviations (SD) for $\sqrt{\langle u^2 \rangle}$, a bead certainly appears to undergo similar thermal motions when affixed to either an F-actin node or an extracellular glycophorin C domain. This is fully consistent with the 4.1-mediated connectivity between these proteins (Fig. 1 *A*). Moreover, the network appears homogeneous in its elasticity because the SDs are small compared to the averages, and are also essentially the same as for immobilized beads.

The scale of measured fluctuations appears consistent with known structural features of the network. Spectrin should be flexible; it has a small persistence length, l_{sp}, of ~5-20 nm (Stokke et al., 1986; Discher et al., 1998) relative to both its contour length ($L_{sp} \approx$ 200 nm for the folded

TABLE 2 Average root-mean-squared displacements, $\sqrt{\langle u^2 \rangle}$, of beads on unstrained portion of cell with maximum corrections for bead wobble (see Appendix 1) and possible zero-point noise

	$\sqrt{\langle u^2 \rangle}$ (nm)		
Experiment	Measured (±SD)	Wobble-Corrected Average	Zero Point-Corrected Average
Glycophorin C (>40 beads)	36 ± 6.6	26	19
F-actin (>40 beads)	34 ± 6.6	24	17

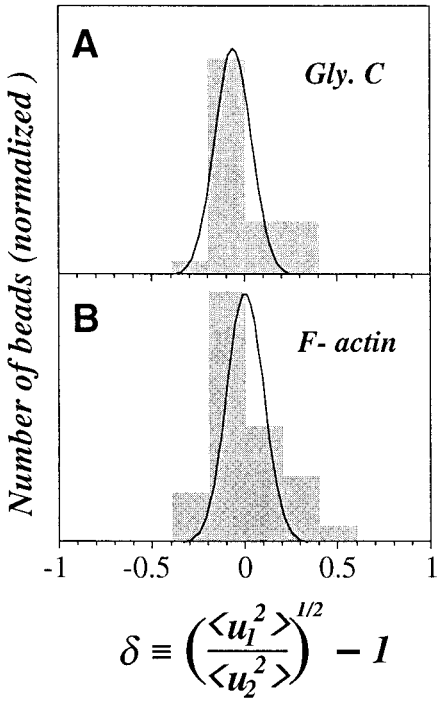

FIGURE 6 Directional dependence of network fluctuations for individual beads on the outer spherical contour of aspirated cells. If fluctuations are isotropic, $\delta \equiv 0$. It is found that $\delta = 0.07 \pm 0.10$ for glycophorin C (*A*) and $\delta = 0.003 \pm 0.19$ for F-actin (*B*).

tetramer) and the average inter-actin spacing ($\xi \approx$ 60-80 nm; e.g., Byers and Branton, 1985). Such values are in general agreement with in situ stretches of the network which are estimated to reach $\lambda_{max} \sim L_{sp}/\xi \approx$ 2-3.

Table 2 also gives corrections for a maximum bead wobble that is conceivably introduced by the finite length tether used here (see Appendix 1). Another systematic correction that might well be considered is the "zero-point" fluctuations of ~7 nm for immobilized beads (Table 1). Altogether, measurements of $\overline{\sqrt{\langle u^2 \rangle}}$ with or without wobble- and zero-point corrections yield final averages of

$$\overline{\sqrt{\langle u^2 \rangle}} = 18^* - 35 \text{ nm}. \quad (1)$$

Where the asterisk (*) denotes the maximally corrected average. Despite the range, such fluctuations are comparable to L_{act} and are certainly significant on the scale of the network mesh size $\xi \approx$ 60-80 nm.

Thermal fluctuations in the network are thus constrained, if only weakly, by the structured softness or elasticity of the network. Given that triangulated networks have sixfold symmetry and therefore should appear isotropic to quadratic order in their elasticity (e.g., Landau and Lifshitz, 1959; Discher et al., 1997) any anisotropy in the fluctuations can, in principle, provide further insight into network structure. Fig. 6 shows histograms and simple Gaussian fits of the isotropy measure $\delta \equiv [\sqrt{\langle u_1^2 \rangle}/\sqrt{\langle u_2^2 \rangle} - 1]$. The determined averages are dominated by standard deviations of 10-20% on this normalized scale and are at or below the noise level of the present measurements. Hence, the elastic properties of the undeformed network appear essentially isotropic.

Elastic modulus estimates based on thermal fluctuations

Autocorrelation analyses of the video-rate data (e.g., Fig. 4 *B*) show a discontinuous jump from a finite value to zero within the period of a single video frame (not shown). Time constants for thermal motions of the bead are therefore well below the collection rate of the intensified camera, making the frequency response of the network and its dynamic viscoelasticity inaccessible by the present approach. A time series of displacement datapoints would nonetheless appear to constitute a statistically independent ensemble and can thereby provide insight into the frequency-independent elasticity.

Application of the equipartition theorem to a strictly two-dimensional and isotropic (or sixfold symmetric) elastic solid is a classical problem of equilibrium statistical mechanics (Chaikin and Lubensky, 1995). Starting with a general correlation function for displacements and a suitable Fourier transform of the small-strain Hamiltonian for a finite segment of solid, Appendix 2 summarizes the relevant equipartition theorem applied to normal elastic modes. The calculation concludes with an integral transformation back to real space that ultimately relates the effective spring constant of the network to both the thermally averaged displacement vector, $\langle \vec{u}^2 \rangle \equiv \langle u_1^2 + u_2^2 \rangle$, and the wavenumber cutoffs for both small fluctuations, $\sim a^{-1}$ and large fluctuations, $\sim \Lambda^{-1}$:

$$k_{eff} = k_B T \frac{\ln(\Lambda/a)}{2\pi} \langle \vec{u}^2 \rangle^{-1} \quad (2)$$

The effective elastic constant is further shown (Appendix 2) to be related, in general, to the shear elastic modulus, μ, and the bulk modulus, K_a, of the elastic solid through $k_{eff} = [\mu(K_a + \mu)]/(K_a + 2\mu)$. Because the network is both embedded in and attached to incompressible fluids (i.e., cytosol and lipid bilayer), one could consider the dilational modes of the network fluctuations to be minimal compared to the in-plane shear modes; in this case, $k_{eff} \approx \mu$. Previous work on the red cell network has suggested, however, that $K_a/\mu \gtrsim 2$ (Discher et al., 1994; Mohandas and Evans, 1994; Boey et al., 1998; Discher et al., 1998); in such a case, $\mu \lesssim 1.33\ k_{eff}$.

Additional uncertainty arises with numerical estimates for the integration limits or cutoffs. To start with, a could range from the persistence length of spectrin l_{sp} to other local length scales, notably ξ; these quantities were listed as ranging from 5 to 80 nm. Our finding that bead fluctuations are essentially isotropic on the spherical contour of mem-

brane (of measured diameter range $D_s \approx 4$-6 μm), indicates that the aspirated projection of membrane (of length $L \approx (0.2 - 1.5)D_s$ in these experiments) is not a significant perturbation to either a or Λ. This further implies that a relevant measure of Λ is certainly no larger than the outer spherical contour, D_s. Physically, the longest relevant wavelength would seem likely to be set by over-damped viscous coupling. A range for $[\ln(\Lambda/a)/2\pi] \approx 0.6$-1.1 is thus estimated. Substituting this and additional quantities above into Eq. 2 allows an estimate of the shear modulus:

$$\mu \approx (0.6\text{–}1.5)k_B T\langle \vec{u}^2\rangle^{-1} \quad (3)$$

Measured fluctuations (Eq. 1) thus lead to a very reasonable if broad range for μ:

$$\mu = 0.001\text{–}0.01^* \text{ pN/nm} \quad (4)$$

The lower value is obtained with uncorrected measures of the thermal motions and, effectively, an incompressible network having normal modes bounded by both the network mesh size $a = \xi$ and $\Lambda = D_s \approx 4$ μm. The upper range not only includes fully corrected measures of the thermal motions (denoted by the asterisk per Eq. 1) and a finite K_a, but also normal modes bounded by both the persistence length of spectrin, $a = l_{sp}$, and $\Lambda = D_s \approx 6$ μm. Clearly, the two-dimensional shear modulus estimates of Eq. 4 are consistent with the order of magnitude estimate given in the Introduction.

The estimations preceding Eq. 4 highlight both the reasonableness of the measurements and limitations of interpretation. Beyond better methods, a better statistical mechanical model that clarifies relevant length scales (notably a and Λ) and perhaps dissipative couplings needs to be developed. Some progress in both directions has recently been made by Helfer et al. (2000) through the use of micron-size beads that would, unfortunately, be inappropriate for the present membrane studies.

Micropipette-deformed network: anisotropic strain state

To more fully probe and understand network fluctuations in a micropipette-deformed membrane, an accurate picture of the network's deformation state is needed. Fortunately, a relatively clear, experiment-rooted understanding of membrane network deformation within micron-diameter pipettes has recently emerged. Early theories (Evans, 1973) were based on a simplifying assumption of surface incompressibility and suggested that the network was stretched in the axial (*1*-) direction of the micropipette by a factor of 2 to 3 along much of the aspirated projection. However, a finite K_a for the network was more recently demonstrated by use of fluorescence-imaged microdeformation wherein the network was prelabeled with various fluorescent probes before cell aspiration (Discher et al., 1994). Subsequent analyses (Discher and Mohandas, 1996; Discher et al., 1998) together with photobleaching experiments (Lee et al., 1999) lead to axisymmetric profiles for spectrin network stretching (λ_1 and λ_2) that indeed reached maximum values of 2 to 3 along much of a typical aspirated projection (Fig. 7 *A* and *B*). Furthermore, circumferential contractions in the *2*-direction ($\lambda_2 < 1$) suggested a simple and useful measure of the local, anisotropic strain state: $E_s \equiv \lambda_1/\lambda_2 - 1$ (per Evans and Skalak, 1980). This local measure of post-deformation aspect ratio or shear strain additionally shows that strain profiles versus (z'/R_p) from multiple experiments and simulations can be collapsed onto a single, nearly straight curve (Fig. 7 *C*). As a static measure of network anisotropy, E_s is analogous to the previously defined δ (Fig. 6) that characterizes anisotropy in thermodynamic fluctuations. However, δ is certainly more revealing of the spectrin-actin network's intrinsic rather than externally imposed response.

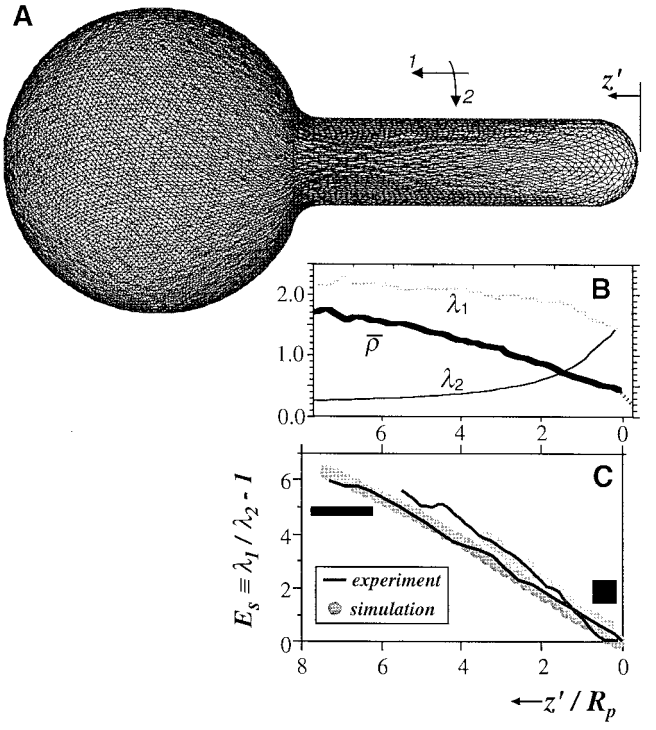

FIGURE 7 Deformation state of the network in aspiration. (*A*) Simulated network from Discher et al. (1998). (*B*) Experimentally determined relative density and direction-dependent extension or stretch profiles along the aspirated projection (Discher and Mohandas, 1996). (*C*) Superposition of shear strain profiles from both experiment and simulation. Collapse of the various results on to a single curve, within 10% error typical of experiment, indicates that the strain anisotropy measure E_s is nearly independent of projection length. Two small black parallelepipeds schematically indicate the local deformation state of the network.

Micropipette-deformed network: anisotropic fluctuations

To explicitly connect local strain anisotropy E_s to fluctuation anisotropy δ, thermal motions of fluorescent beads affixed to F-actin were tracked in cell ghosts at various points along a micropipette-aspirated projection (Fig. 8 *A*). Near the tip of the aspirated projection, particle fluctuations such as those shown in the rightmost panels of Fig. 8 *B* appeared isotropic and very similar in magnitude to those on the outer contour of membrane. The network is known to be isotropically dilated at the projection's tip (Discher et al., 1994), but the maximum extensions at the tip are always intermediate to the extensions further back, along the length of the projection. Even simulations (e.g., Fig. 7 *A*) with a strain-stiffening spectrin tether model suggest minimal impact on network fluctuations at or near the projection's tip.

In contrast, sample trajectories of particles near the entrance of the micropipette (*left panels* in Fig. 8 *B*) reveal strongly anisotropic fluctuations with axial fluctuations considerably increased. The trend of increasing fluctuations with increasing distance, z'/R_p, from the aspirated projection's tip is highly reproducible between cell ghosts (Fig. 8 *C*). The similar trends in $\sqrt{\langle u_1^2 \rangle}$ and $\lambda_1(z')$ of Fig. 7 *B* are also striking, and the fact that the glass micropipette and the aspirated projection have a constant shape or curvature over this length from $1 \leq z'/R_p \leq L/R_p$ argues against systematic optical distortions. Numerically, the maximum fluctuations are found, either with corrections (denoted by *) or without corrections, to be 38* or 55 $\pm$ 7 nm (near $z'/R_p \sim$ 9-10); these values are $\sim$20 nm or 1.5-2.1*-fold higher than fluctuations on the unstrained contour of membrane (Eq. 1).

Plots of the anisotropy measure δ against z'/R_p show a significant and near-linear increase analogous to the shear strain measure E_s (Fig. 7 *C*). Direct plots of r.m.s. displacements (Fig. 8 *C*) nonetheless appear more revealing and certainly suffer less from possible systematic errors, such as particle wobble (Appendix 1). The correspondence between axial extension profiles and axial fluctuations is mirrored in a trend of weakly suppressed circumferential fluctuations (Fig. 8 *C*), which compares well with circumferential contractions ($\lambda_2 < 1$ of Fig. 7 *B*). However, by any statistical measure, individual $\sqrt{\langle u_2^2 \rangle}$ do not differ significantly from fluctuations on the unstressed outer contour of membrane (Table 2) as represented in Fig. 8 *C* by a dashed line for the mean and a gray zone for S.D.

Micropipette-deformed network: directional elastic constants

To highlight the anisotropy, spatial-dependence, and quasi-Gaussian nature of particle fluctuations, representative distributions $P(u_1)$ are plotted in Fig. 9. The distributions are shown on a logarithmic scale and inverted compared to the distribution of Fig. 2 *B*. Note that $P(u_1)$ is a binned proba-

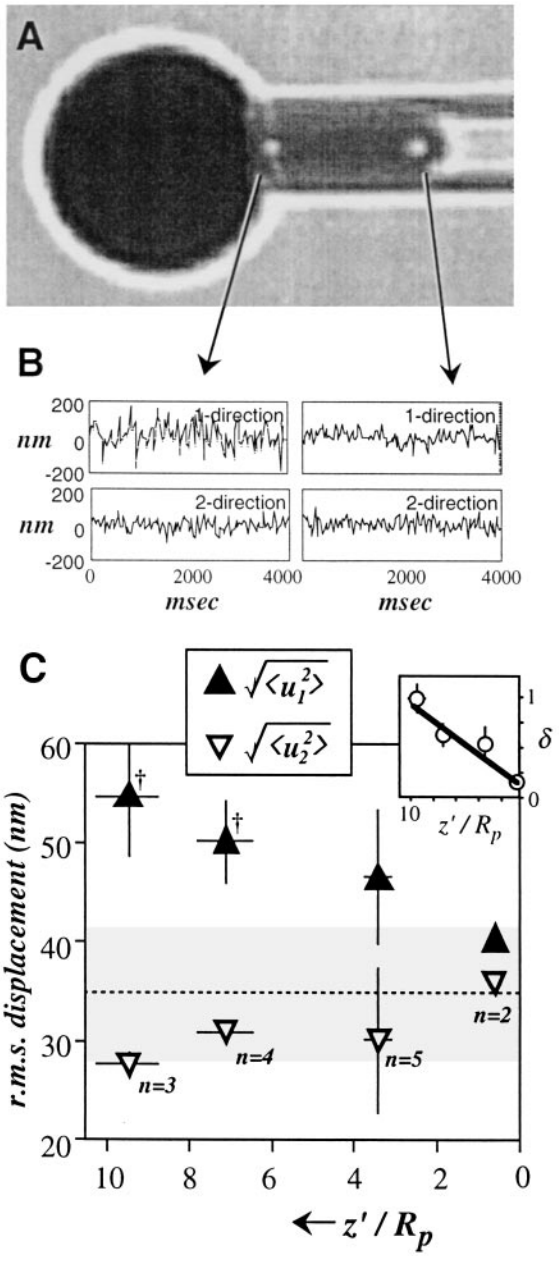

FIGURE 8 Motions of 40-nm fluorescent beads attached to F-actin and located on the aspirated projection of a micropipette-deformed red cell ghost. (*A*) Beads were tracked at various positions along the projection, displaying (*B*) fluctuations that are dependent in magnitude on both direction and position (*C*) on the aspirated projection. In particular, near the micropipette entrance, fluctuations in the axial direction are almost twice those near the aspirated projection's tip. Fluctuations in the circumferential direction, again near the micropipette entrance, are more weakly affected but appear slightly suppressed compared to those near the tip. The upper inset emphasizes the trend by showing that bead fluctuations (uncorrected) are isotropic near the aspirated projection's tip but are increasingly anisotropic toward the entrance of the micropipette. For the 12 cell ghosts examined, the range of projection lengths, L, was 7–10 R_p, where R_p is the radius of the micropipette (0.7-0.9 μm). The gray region corresponds to the $\pm$6.6 nm error in the measurements of bead motions on the unstrained portion of the cell. Error bars in (*C*) correspond to standard deviations for the indicated number of cell ghosts; datapoints that have 95% confidence intervals which do not overlap with the gray region are highlighted with a dagger.

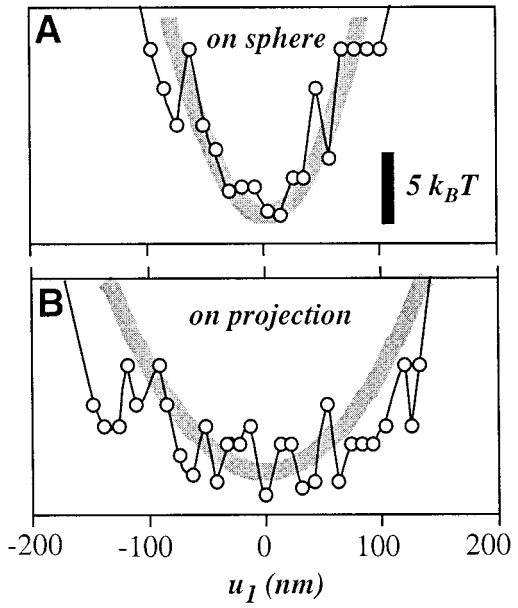

FIGURE 9 Effective potentials obtained from uncorrected thermal displacement probabilities per Eq. 5. In (*A*) the bead was located on the unstrained, spherical portion of the cell outside of the micropipette. In (*B*) the bead was located in the highly strained region at the base of the projection where the fluctuations are greatest. In both cases, thermal motions were binned in intervals ~10 nm wide, yielding continuous probability distributions. Effective spring constants, $k_{1,\text{eff}}$, were determined from quadratic fits to the effective potentials: for (*A*), $k_{1,\text{eff}} = 0.004$ pN/m and for (*B*) $k_{1,\text{eff}} = 0.0015$ pN/nm.

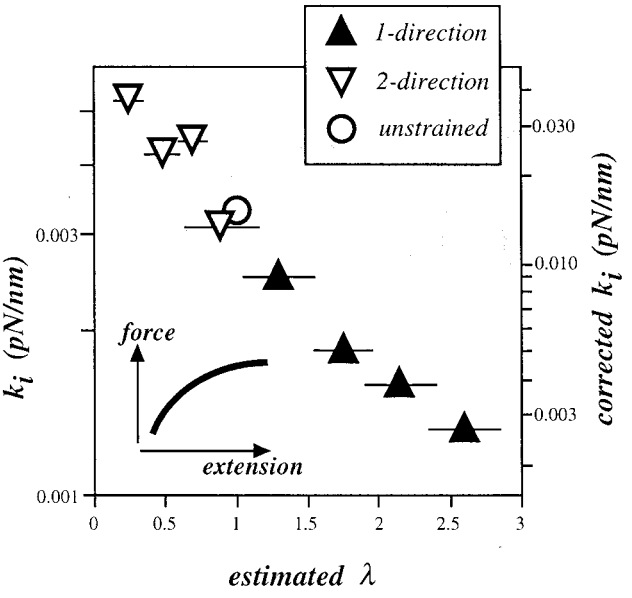

FIGURE 10 Effective spring constant versus estimated network extension ratio (λ_i). Network stretches in the *1*- or *2*-directions were estimated (together with ±SD) from results of the type illustrated in Fig. 7 and were applied to each datapoint of measured fluctuations (Fig. 8). Directional spring constants were determined from the equipartition theorem per Eq. 5b either with or without noted corrections of the r.m.s. displacements (see Appendix 1). The gray region corresponds to the elasticity error introduced by the ±6 nm SD in the measured bead motions on the unstrained portion of the cell; the vertical error bars of Fig. 8 are otherwise omitted. The inset sketch of force versus extension schematically indicates the continuous strain softening that is clearly implicated by the reduced spring constant ($k_{SP} \sim df/d\lambda$).

bility with bin size set by system noise limits of ~±5 nm (per Fig. 2). Distributions are illustrated for a bead either on the unstrained outer sphere or in a highly strained region of the aspirated projection, near the micropipette entrance (respectively, Fig. 9 *A*, and *B*). Scaled by k_BT, this inverted-log representation generically defines an effective potential

$$V_i(u_i) = [\text{constant} - k_BT \ln P(u_i)] \tag{5a}$$

which we approximate as a harmonic function and apply the equipartition theorem (per Eq. 3):

$$\tfrac{1}{2} k_{i,\text{eff}} \langle u_i^2 \rangle = \tfrac{1}{2} k_BT \tag{5b}$$

The results of Fig. 8 *C* for average r.m.s. directional displacement are used to estimate effective elastic constants. Comparing the *1*- versus *2*-directions at the same distance from the tip, the difference between the local compliances—with maximum corrections made for particle wobble and the zero-point anomaly—can reach 10-fold near the micropipette entrance for projection lengths of L/R_p = 8-10. Without correction, this difference averages nearly fivefold. As plotted in Fig. 10 versus estimated extension ratios (using Fig. 7 *B*), calculations of elastic constants either with corrections (denoted by *) or without corrections show that the maximum measured increase in compliance relative to the unstrained contour of membrane is found (near $z'/R_p \sim$ 9-10) to be 2.25 or 4.4(*). The network is directionally strain-softened (Fig. 10, *inset*). For perspective, orthogonal stiffnesses in the spectrin-actin cortex of the outer hair cell have been measured (Tolomeo et al., 1996) to be in a ratio of (0.0030 pN/nm / 0.0005 pN/nm) = 6, which is credibly attributed to stiff actin filaments that are crosslinked in a perpendicular direction by much softer spectrin chains. Although remarkably similar in magnitude, the anisotropic elasticity elucidated here is clearly distinct in that it reflects a strain-induced softening.

DISCUSSION

Motivated in part by the pathological consequences of network defects such as spectrin deficiencies (Waugh and Agre, 1988; Mohandas and Evans, 1994), a number of experimental techniques and theoretical analyses have been developed to quantify network elasticity. Micropipette methods emerged early: incremental aspiration of a projection of membrane has led to shear modulus estimates in the range of μ = 0.004 to 0.010 pN/nm (Evans, 1973; reviewed in Hochmuth and Waugh, 1987), with the most accurate

measures reportedly being at the upper end of this range (Evans et al., 1984). A somewhat lower μ (=0.002-0.003 pN/nm) was recently estimated from laser tweezer-imposed stretching of red cells (Hénon et al., 1999). Still lower values of μ, renormalized by thermally excited membrane bending modes, have also been estimated from equipartition analyses of undulations (Strey et al., 1995). Important distinctions in strain regimes should be pointed out. Maximum network strains or extension ratios (λ_{max}) in the cell network typically reach values of two or more toward the base of a micropipette-aspirated projection of membrane (Discher and Mohandas, 1996; Lee et al., 1999), whereas laser tweezer and undulation measurements appear confined to small strain regimes and certainly include significant membrane bending contributions. Nonetheless, the present estimates here of $\mu \approx 0.001$-0.010 pN/nm (Eq. 4) are consistent with small-strain and large-strain measurements.

Although local determinations of $k_{i,eff}$ on a micropipette-aspirated projection ignore all boundary conditions and any wavelength cutoffs, geometrically accurate Monte Carlo simulations of the type shown in Fig. 7 *A* predicted suppressed fluctuations in the circumferential direction (Discher et al., 1998). This is in qualitative agreement with experiment and had been explained as arising from interchain sterics. Moreover, the effective strain-stiffening in the strongly contracted circumferential direction may well be the origin of the higher μ value reported with micropipette methods. Unlike experiments, however, no softening was seen in simulation in the strongly stretched axial direction. The difference likely reflects the use, in simulations, of a strain-stiffening molecular tether model (i.e., worm-like chain). The finding that the extensional forces on spectrin chains near the micropipette entrance are distributed over a range of ~1-10 pN may nonetheless prove realistic. Indeed, previous aspiration experiments (Waugh and Evans, 1979) show that the aspiration pressure (ΔP) and aspirated projection length (L/R_p) are nearly proportional, allowing extrapolation to $L/R_p \sim 8$, where fluctuations become significantly deformation-enhanced (Fig. 8 *C*). Thus, the average force on spectrin in the axial direction could be as high as $\bar{f}_{max} \approx (\frac{1}{2}\ \Delta P R_p)\ \xi \approx 4$ pN. Whether such forces, on experimental time scales, are sufficient to drive either intermolecular or intramolecular network disruptions is discussed next.

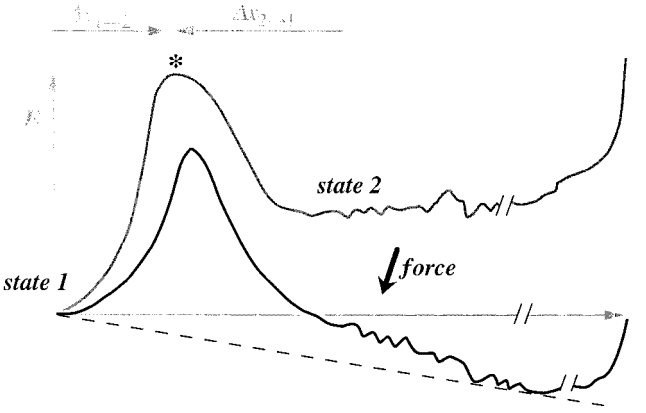

FIGURE 11 Free energy landscape for a two-state transition under force. Applied force tilts the profile from, for example, the associated state to the dissociated state. To the right of the indicated breaks are states irrelevant to protein dissociation but important to protein unfolding. The transition state (*) is separated, in this 1D model, from the two most energetically important states by the indicated linear distances.

Inter and intramolecular transitions as possible bases for deformation-enhanced fluctuations

The spectrin-actin network is clearly a supramolecular assembly of both inter and intramolecular interactions (Fig. 1), any of which might be disrupted under strain. Among protein-protein interactions, some associations more than others seem likely candidates for shifts in equilibrium toward dissociated states (Fig. 11) that collectively generate a softer network. A first candidate to consider for dissociation is spectrin's interaction with actin, which has long been estimated to be weak, with a dissociation constant (K_d) of only ~0.2 mM (Ohanian et al., 1984). However, the lack of any mechanokinetic data together with known stabilizing interactions between spectrin-actin and protein 4.1 (Discher et al., 1995) precludes any detailed consideration of such a forced-dissociation. Purely mechanical arguments for triangulated networks (Appendix 3) nonetheless suggest that the observed softening of 2.25-4.4*-fold (see Results) requires only modest shifts in connectivity: only ~25% fewer spectrin-actin associations (neglecting 4.1) are required to theoretically explain the enhanced fluctuation data. Qualitatively similar effects might be postulated for shifts in spectrin head-to-head associations (i.e., α-spectrin associating with β-spectrin) and other so-called "horizontal" associations within the effective plane of the network. In the transverse, or "vertical" direction, slightly more subtle transitions might have similar effects. For example, stretch-straightened spectrin chains might disrupt band 3's association with ankyrin, or else ankyrin's association with spectrin. Intuitively, such reduced constraints on spectrin should enhance conformational freedom, and thereby fluctuations. Analyses of such processes are again limited by lack of mechanokinetic data for dissociation or re-association.

Distinct from protein-protein interactions, intramolecular transitions might also be considered as contributing to network softening. Side-to-side interactions between spectrin's two α- and β-chains have been speculated to be susceptible to disruption by pico-Newton forces (A. Kusumi and coworkers, personal communication). Moreover, single molecule studies using AFM suggest that any one of the many triple-helical domains in the α- and β-chains of tetrameric spectrin ($m \equiv 76$ domains) can reversibly unfold, either

fully (Rief et al., 1999) or partially (Lenne et al., 2000). Given that a red cell contains $\sim 10^5$ spectrin tetramers and almost 10^7 triple-helical spectrin domains, the presence of a few unfolded domains existing at any instant, in even an undeformed red cell, seems reasonable. An increased number of unfolded domains under a significant stretch of the network seems equally reasonable. Starting with mechano-kinetic considerations below, general criteria for transitions will be outlined. Subsequent discussion will quantitatively illustrate the criteria with detailed though data-limited analyses of α, β-spectrin head-to-head dissociation and spectrin domain unfolding.

Assessing the possibilities: two-state kinetic considerations of single molecules under force

Tension-biased transitions in molecular interactions have been well-documented for irreversible detachment in cell adhesion (e.g., Evans et al., 2001) and for the reversible unfolding of a number of cytoskeletal and adhesion proteins (e.g., Rief et al., 1997; Carl et al., 2001) plus nucleic acid chains (e.g., Liphardt et al., 2001). The kinetics of a two-state transition of a molecule in an external field f takes a familiar form applied, per recent example, by Bustamante and co-workers (Liphardt et al., 2001) to the reversible disruption of single RNA hairpins:

$$\tilde{k}_{1\to 2}(f) = k_m k^o_{1\to 2} \exp\left(\frac{f\Delta x^*_{1\to 2}}{k_B T}\right) \qquad (6)$$

In Eq. 6 the tilde denotes the force-dependence of the rate and k_m supposedly captures specific mechanical effects of couplings to the molecule. The spontaneous (force-free) transition rate is given by $k^o_{1\to 2}$, and the path length from state *1* to the key transition state en route to state *2* is defined as $\Delta x^*_{1\to 2}$ (see Fig. 11). The exponential term in Eq. 6, as described by Evans and Ritchie (1999), decrements the free energy of the transition state by tilting the free energy landscape away from state *1*, thus favoring state *2* (Fig. 11).

A critical implication of Eq. 6 to deformation-enhanced network fluctuations is that, for a postulated reaction to occur, the spontaneous rate $k^o_{1\to 2}$ and $\Delta x^*_{1\to 2}$ must be high enough that imposed forces of $\sim$pico-Newton magnitude cause transitions on experimentally relevant time scales. In terms of inverse time scales or rates, the relevant range here is bounded by the duration of aspiration ($\nu_{min} \sim 10^{-2}$ s^{-1}) and the video rate of measurement ($\nu_{max} \sim 10$ s^{-1}). The spectrin head-to-head interaction appears to be at least one complex that can be explicitly considered: monomeric α-binding to monomeric β-spectrin is well-characterized both structurally and in terms of activation energy profiles (DeSilva et al., 1992). Using recombinant peptides, the dissociation rate of this interaction has been determined to be $k^o_{\alpha,\beta\text{-dissocn}} = 3.4 \times 10^{-4}$ s^{-1} (23°C). Furthermore, this complex is known to involve helices (of length $\leq$5) nm and interactions that qualitatively resemble those of spectrin's triple helical folds for which Rief et al. (1999) estimated $\Delta x^*_{1\to 2} \approx$ 1-3 nm from simulated fits of unfolding. Based on these numbers and the pico-Newton forces on spectrin during aspiration, Eq. 6 would suggest that the bare rate is too slow to be accelerated to a relevant rate ($> \nu_{min} \sim 10^{-2}$ s^{-1}). However, having already postulated that the α,β-spectrin dissociation might well resemble domain unfolding because of the common helix-helix interactions, the fact that each spectrin tetramer contains $m = 76$ triple-helical domains heightens, in comparison, the probability of unfolding.

Before concluding this discussion section by explicitly including the number of unfoldable spectrin domains in Eq. 6, we note that the forward ($1 \to 2$) process of Eq. 6 also generally implies the existence of the reverse $2 \to 1$ transition (see Fig. 11). For this, the same question of time scale applies, of course, but if forward and reverse rates (further qualified below) are as fast as the measurement resolution, the $1 \to 2 \to 1 \to 2 \to 1 \ldots$ process will naturally introduce system fluctuations.

Spectrin domain unfolding and micro-ensemble fluctuations

Spectrin domain unfolding under chain extension certainly appears well-demonstrated, but it has only been documented at relatively high extension rates (of $\sim$nm/ms) and not yet under a constant, time-invariant force, as would be most useful for straightforward assessments using Eq. 6. Furthermore, "force-clamp" loading would also seem the most insightful and relevant to fluctuations in sustained network deformations, such as those on a cell projection held at fixed ΔP.

Force-clamp measurements of single molecule transitions have only recently been made. Individual RNA hairpins that are ordinarily zipped up (folded) via a series of hydrogen bonds ($>$30) have been studied under a fixed force imposed by an optical trap (Liphardt et al., 2001). The many hydrogen bonds in an RNA hairpin are qualitatively similar to those in the three α-helices of each spectrin domain, and so the unfolding-refolding of RNA is illustrative of what might be found with spectrin. With RNA, it was shown that under a set force of only $f_{1/2} = 14.5$ pN, the hairpin spends half of its time unfolded or unzipped and half of its time fully folded; equivalently, $\tilde{k}_{1\to 2}(f_{1/2}) = \tilde{k}_{2\to 1}(f_{1/2})$ per Eq. 6. Although the 18-nm-length jumps between folded and unfolded states were "unresolvably fast ($<$10 ms)," (Liphardt et al., 2001), the time spent in either state appeared exponentially distributed and lasted as long as seconds. Such slow fluctuations contrast with the rapid axial fluctuations elucidated by our molecular scale beads in the highly strained spectrin network (*top left panel* of Fig. 8 *B*). In addition to the obvious RNA versus protein difference, system size differences must not be overlooked: the spectrin

network, in the crudest approximation, is a finite system of N two-state systems, all undergoing noncooperative transitions. For such a system, any given *overall* extension-state will then be much shorter-lived than the single domain substates. The important, intuitive conclusion is that fluctuation frequencies at the ensemble scale (in a force-clamp at least) grow with system size N.

The equipartition theorem of Appendix 2 explicitly incorporates maximum system size through the cutoff wavelength Λ and also suggests working definitions of the network micro-ensemble probed by the fluctuating bead. In a first approximation, N should be the number of spectrin domains within an area delimited by Λ^2 (as large as μm^2 in scale); however, as Hill points out (Hill, 1985), the physically cooperative statistical mechanics of two-dimensional multistate systems such as the network generally require computational methods for accurate descriptions. Given the directional nature of the deformation-enhanced fluctuations, N might be crudely divided by ~ 2 for the two orthogonal directions. Regardless, relevant system sizes span a considerable number of folded spectrin domains since each spectrin tetramer contributes $m = 76$ triple helical domains each capable of two or more transitions. In terms of the number of spectrin tetramers, $n = N/m$, the system size needed for unfolding to contribute to network fluctuations can be operationally defined using Eq. 6:

$$n = \frac{1}{m}\,\nu_{\max}/k_m k^o_{1\to 2}\exp\left(\frac{f\Delta x^*_{1\to 2}}{k_B T}\right) \qquad (7)$$

In addition to estimating $\Delta x^*_{1\to 2} \approx$ 1-3 nm, Rief et al's simulated fits of average forces for full unfolding provide values for $k_m k^o_{1\to 2}$ that range from $2.5 \times 10^{-3}\ s^{-1}$ to $1.7 \times 10^{-7}\ s^{-1}$. (Note that the previous $k^o_{\alpha,\beta\text{-dissocn}} = 3.4 \times 10^{-4}\ s^{-1}$ is within this broad range and consistent with like interactions in spectrin unfolding and association). For $f =$ 0 pN, Eq. 7 yields the minimal number of spectrin tetramers for which unfolding enters the measurements (without yet considering refolding): $n_{f=0} \approx 4 \times 10^{1\text{-}5}$. Under aspiration-imposed forces that could locally reach $\bar{f}_{\max} \approx 4$ pN (see Results), the exponential term in Eq. 7 decreases n by up to 20-fold to: $n_{\bar{f}_{\max}} \approx 2 \times 10^{0\text{-}4}$. The lower range is obviously very local, on a length scale of just the mesh size ξ, whereas the upper range is 10-fold smaller than the number of spectrin tetramers per red cell (e.g., Byers and Branton, 1985). Assuming for now that domain refolding is not rate-limiting, unfolding under force could thus enhance fluctuations, and on the fastest time scale of experimental detection. Fluctuation amplitudes can also be shown consistent with a very moderate amount of unfolding. Depending on the force, reported length gains in unfolding single spectrin domains range from about 15 to 30 nm for partial or full unfolding, respectively. In comparison, the maximum measured increase in fluctuations was shown in Fig. 8 *C* to be $\sqrt{\langle u_1^2\rangle} - \sqrt{\bar{u}^2} \approx 55\text{ nm} - 35\text{ nm} = 20\text{ nm}$.

Discussion of spectrin domain unfolding requires further qualification. First, partial unfolding is intuitively anticipated to be more labile than full unfolding. Although Rief et al. (1999) reported that "no intermediate states can be seen," thus calling into question the numerical accuracy of the earliest forced unfolding measurements, partial unfolding indeed appears to require $\sim$⅓ less force at a given rate (Lenne et al., 2000). Kinetic parameters have not yet been estimated, however. It is also not yet firmly established how an AFM cantilever of typical stiffness 10 pN/nm, or $\sim$10,000-fold stiffer than the spectrin network, influences the measured rate constants (e.g., through k_m in Eq. 6). Evans and Ritchie (1999) have concluded that measurement system compliance in single molecule experiments can have a considerable effect on rate-dependent transition forces. Given the present caveats on spectrin unfolding, it is intriguingly plausible that local unfolding of a few of the red cell's $\sim 10^7$ triple-helical domains underlies deformation-enhanced fluctuations. Appendix 4 elaborates more fully on equilibrium fluctuations in unfolding of a single spectrin chain: refolding (which takes "less than a second" (Rief et al., 1999)) and other key remaining issues are considered there. The calculations ultimately emulate the strain-softened increase in extensional forces illustrated in the inset to Fig. 10. The calculations are intended, however, to be illustrative and generally relevant—with different parameters—to mechanochemical equilibria such as spectrin heterochain dissociation and re-association under tension.

CONCLUSIONS

Thermal fluctuations of actin protofilament nodes, as measured by nano-particle tracking, appear highly localized and consistent with the macroscopic elasticity of the erythrocyte network. The in-plane fluctuations sweep out a projected area that is a significant fraction of the network's internodal spacing. The fluctuations are also 2D isotropic, suggesting that defects in the network are not extreme. Moreover, cell deformation in a micropipette directly affects network fluctuations, and in a manner that directly parallels the local deformation state of the network within the pipette. In the contracted circumferential direction fluctuations are relatively suppressed, whereas in the extended axial direction fluctuations are measurably enhanced and indicative of network strain-softening. Deformation-enhanced fluctuations could reflect a range of molecular processes, including dissociations that reduce connectivity and forced-equilibrium processes such as full or partial unfolding of a few of the red cell's $\sim 10^7$ spectrin repeats. Kinetic considerations and an analytical two-state model partially quantifies such possibilities, although additional single molecule results and biochemical data are certainly needed.

APPENDIX 1

Wobbling of a molecularly tethered nano-particle

In terms of a tether length, l_t, particle radius, R, and angle, θ, between the tether and the planar membrane surface, the projected distance between the tethering origin and the particle centroid is simply $s = (l_t + R)\cos\theta$. This distance has a variance

$$\sigma_s^2 = \{\langle\cos^2\theta\rangle - \langle\cos\theta\rangle^2\}(l_t + R)^2 \qquad \text{(A1.1)}$$

Since $\langle\cos\theta\rangle = 0$, $\langle\cos^2\theta\rangle = \int_{\theta_{min}}^{\pi-\theta_{min}} \cos^2\theta \cdot d\theta$, and $\theta_{min} = \sin^{-1}(R/(l_t+R))$, we obtain

$$\langle\cos^2\theta\rangle = \frac{1}{2}\left[\pi - 2\sin^{-1}\left(\frac{R}{l_t + R}\right)\right] \qquad \text{(A1.2)}$$

The r.m.s. error due to the "wobble" effect is estimated to be

$$\sqrt{\sigma_s^2} \le (l_t + R)\sqrt{\langle\cos^2\theta\rangle} \qquad \text{(A1.3)}$$

Assuming $l_t \le 10$ nm, $R \approx 20$ nm, $\sqrt{\sigma_s^2} \le 10$ nm. This is comparable to the system noise (Table 1) and is much smaller than r.m.s. fluctuations of network-attached beads. Moreover, since the calculation is for a bead constrained to fluctuate in a plane rather than a half-space, it is also a worst-case estimation.

APPENDIX 2

Elasticity and fluctuations in a two-dimensional isotropic solid

Following Chaikin and Lubensky (1995), the correlation function for material displacements is generically denoted in Fourier space as $G_{ij}(\mathbf{q}) = A^{-1}\langle u_i(\mathbf{q})u_j(\mathbf{q})\rangle$, where A reflects the size of the system. This thermal average is evaluated by use of the Fourier-transformed strain energy or Hamiltonian $H_{elastic}(\mathbf{q})$ which, for a two-dimensional elastic solid, is expressed in terms of just two elastic moduli, the bulk modulus, K_a, and the shear modulus, μ. The equipartition theorem is then used, assigning k_BT per normal mode to arrive at:

$$G_{ij}(\mathbf{q}) = k_BT(K_a + \mu)^{-1}q^{-2}\hat{q}_i\hat{q}_j + k_BT\mu^{-1}q^{-2}(\delta_{ij} - \hat{q}_i\hat{q}_j) \qquad \text{(A2.1)}$$

The first term consists of the longitudinal fluctuations, and the second term consists of the transverse fluctuations. Defining the displacement vector as $\langle\mathbf{u}^2\rangle \equiv \langle u_1^2 + u_2^2\rangle$, we transform back into real space:

$$\begin{aligned}\langle\mathbf{u}^2\rangle &= \int\int \frac{d^2q}{(2\pi)^2}\,Tr[G_{ij}(\mathbf{q})] \\ &= k_BT\{(K_a + 2\mu)/[\mu(K_a + \mu)]\}\,\frac{1}{2\pi}\int_{\pi/\Lambda}^{\pi/a}\frac{\mathbf{q}\cdot d\mathbf{q}}{q^2} \\ &= k_BT(K_a + 2\mu)[\mu(K_a + \mu)]^{-1}\,\frac{\ln(\Lambda/a)}{2\pi} \qquad \text{(A2.2)}\end{aligned}$$

The integration limits a and Λ are introduced as fluctuation cutoffs, ensuring convergence of the integration as needed for a finite size system.

APPENDIX 3

Reductions in network connectivity and elasticity

Local shifts in the equilibrium number of crosslinks toward dissociation (Fig. 11) and away from the unstrained natural state (of crosslink density ϕ^0) result in a decreased network connectivity or crosslink density ϕ. This quantity is most simply proportional to network elasticity for cytoskeletal gels (Stokke et al., 1986) and might even be directionally reduced under local forces or strains. For example, the projected crosslink density, ϕ_1^o, in the *1*-direction would decrease with force. Assuming a nearly perfect lattice to start with, the elasticity is typically found to be in offset proportion to crosslink density, i.e.,

$$k_{1,eff} \approx b + m\phi_1 \qquad \text{(A3.1)}$$

In this, $b \approx -m\phi_{1c}$ and $m \approx k_{1,eff}/(\phi_1^o - \phi_{1c})$ are both set by a rigidity percolation limit, ϕ_{1c}, that depends, in general, on the particular network Hamiltonian (Feng and Sen, 1984). In the present Results, $k_{1,eff}$, was shown to be reduced by as much as 2.25 − 4.4-fold under deformation. For a range of triangulated spectrin-like networks of Hookean springs (Hansen et al., 1997; Boey et al., 1998) $\phi_{1c} \approx \frac{2}{3}\,\phi_1^o$ so that $\phi_1 \approx (0.74\text{-}0.81)\phi_1^o$. Such a network is still well-connected with the local equilibrium shifted only modestly (by 19 to 26%) toward the dissociated state.

APPENDIX 4

Further considerations of equilibrium fluctuations under tension of a spectrin-like chain with *N* internal two-state transitions

Whether multidomain proteins such as spectrin, titin, or Ig-cell adhesion molecules (Carl et al., 2001) unfold within their normal function is among the central questions raised by the dozens of recent reports of single molecule extension and unfolding. In micropipette deformation of the red cell, it appears clear that the spectrin network sustains average extensional forces that reach pico-Newtons in magnitude. From in vitro experiments, it is also clear that spectrin undergoes unfolding, both full (Rief et al., 1999) and partial (Lenne et al., 2000), as well as refolding. Additional intra-spectrin transitions might include α, β strand separation (Tomishige et al., in preparation). From the rate-dependent studies done to date on single chains, however, it is not yet clear whether intra-spectrin transitions, both forward and reverse, can occur on experimental time scales under constant tensions of pico-Newton magnitude. In what follows, the unfolding-refolding of spectrin that is equilibrated under a fixed imposed tension will be coupled analytically to a polymer elasticity model. The approach is closely related to nonequilibrium numerics of Rief et al. (1998) and an equilibrium Ising model calculation for a stretch transition in DNA (Ahsan et al., 1998). Only two-state unfolding rather than multistate unfolding is considered due to the lack of experimental numbers for the latter.

Prior discussion of the full unfolding of spectrin domains under pico-Newton forces demonstrates that transition rates—based on values of $k_{1\to2}^o$ and $\Delta x_{1\to2}^*$ (see Eq. 6) from AFM—could be faster than the measured frequency of deformation-enhanced fluctuations (Fig. 8 *B*). A considerable number, *N*, of spectrin domains had to be considered, but it was emphasized that each spectrin tetramer contains and thus contributes $m = 76$ triple helical domains. Discussion of refolding rates requires, in comparison, more speculation because experimental determinations of $k_{2\to1}^o$ and $\Delta x_{2\to1}^*$ are not yet available. Equilibrium considerations for a stable protein fold clearly require, however, that $k_{2\to1}^o \gg k_{1\to2}^o$, so that refolding is strongly favored. Second, given the condensed nature of folded proteins, the key transition state (Fig. 11) may well be closer to the folded state than the unfolded state, but the separation of these key states is not so great, i.e., $|\Delta x_{2\to1}^*| \sim \Delta x_{1\to2}^*$. Careful AFM-refolding studies of titin's I_{27} domain indeed identify a key condensed denatured state that is separated from the

transition state by 2-3 nm (Carrion-Vazquez et al., 1999). Thus, in later calculations, we will suppose that $\Delta x^*_{2\to1} = -2.5$ nm for full unfolding of spectrin; in absolute value, this is in the upper range of spectrin's $\Delta x^*_{1\to2}$ = 1-3 nm, and the negative sign for $\Delta x^*_{2\to1}$ leads to a decrease in $\tilde{k}_{2\to1}(f)$ with increasing extensional force ($f \geq 0$).

Extension of the unfolded chain beyond the condensed denatured state must also be considered as a third factor: it might indeed seem likely that an unfolded chain that is also stretched would never refold. The basic length scale that a forcibly extended chain must be compared to is $\Delta\Delta x = \Delta x^*_{1\to2} - \Delta x^*_{2\to1}$. If a chain conformation is longer than this it will not refold, whereas a chain conformation shorter than $\Delta\Delta x$ is reasonably assumed capable of refolding. Assuming the unfolded state (of contour length $L_u \approx 30$ nm) has the linear response of a simple polymer of persistence length p_u (~0.5 nm), the average end-to-end length under a fixed force is $\langle x\rangle = \frac{2}{3}\, p_u L_u f/k_BT \approx (3\text{ nm/pN}) \times f$. Importantly, however, chain length fluctuations about the average state of such a forcibly extended chain are considerable and can be estimated with Eq. 5b: $\sqrt{\langle u^2\rangle} = \sqrt{k_BT/k_{eff}} = \sqrt{p_u L_u} \approx 4$ nm. Indeed, the force-extension curves of both Rief et al. and Lenne et al. certainly exhibit considerable fluctuations between unfolding peaks, qualitatively consistent with chain fluctuations in the unfolded length if not simply instrument noise. For forces of f = 3-4 pN, the relevant fraction of chain conformations of length $\Delta\Delta x$ or smaller is readily estimated from a Gaussian distribution of states to be $\tilde{\omega} \sim$ 0.1-10%. The frequency of refolding is thus reduced by this same percentage. Nonetheless, refolding of unfolded domains on a time scale of seconds, even when they are held extended to about half their contour length, is well-documented with titin's I_{27} domain (Carrion-Vazquez et al., 1999). The force-clamp experiments on RNA hairpins (Liphardt et al., 2001), where lengthening transitions of 18 nm are observed, also clearly establish the ability of forcibly extended molecules to refold against a force on time scales of seconds.

Altogether, the single domain refolding rate given by $\tilde{\omega}k^o_{2\to1}\exp(f\Delta x^*_{2\to1}/k_BT)$ seems, from the estimates above, comparable in magnitude at mean forces of $\bar{f}_{max} \approx$ 3-4 pN to the unfolding rate $k^o_{1\to2}\exp(f\Delta x^*_{1\to2}/k_BT)$. Comparing to ν_{max}, refolding rates in a size-N system should not prove any more rate-limiting than unfolding. Given the likelihood that a sufficient number of spectrin domains could unfold and refold on time scales smaller than even the highest data collection rate of the present studies, we finish with a calculation of chain length fluctuations for a spectrin-like chain held under constant f. For simplicity and consistent with analyses of the RNA force-clamp experiments (Liphardt et al., 2001), we neglect the force-dependent refolding rate factor $\tilde{\omega}$ (<100%) introduced above.

Equilibrium under a fixed force generates a fraction of unfolded domains, $\tilde{\theta}_U$, calculated from the rate constants of unfolding and refolding (Eq. 6). The expression has a standard hyperbolic form:

$$\tilde{\theta}_U = \frac{(k^o_{1\to2}/k^o_{2\to1})\exp(f\Delta\Delta x/k_BT)}{1 + (k^o_{1\to2}/k^o_{2\to1})\exp(f\Delta\Delta x/k_BT)} \qquad \text{(A4.1)}$$

Any systematic measurement factor such as k_m of Eq. 6 cancels. The ratio $k^o_{1\to2}/k^o_{2\to1}$ is the equilibrium constant and depends on both T and the previously identified "disbonding" force, $f_{1/2}$, defined as:

$$(k^o_{1\to2}/k^o_{2\to1}) = \exp\left[-\frac{f_{1/2}\Delta\Delta x}{k_BT}\right] \qquad \text{(A4.2)}$$

Since $k^o_{2\to1} \gg k^o_{1\to2}$ for a stable fold, $f_{1/2}\Delta\Delta x$ must be greater than k_BT. However, $f_{1/2}$ is certain to be much smaller than the 20-35 pN required to unfold spectrin repeats under the rapid extension rates (nm/ms) used in AFM (Rief et al., 1998). Recall that the hairpin loop of RNA had $f_{1/2} \approx$ 14.5 pN. Defining $\tilde{F}$ and $\tilde{U}$, respectively, as the number of folded and unfolded repeats, then $\tilde{F} = \tilde{U}$ and $\tilde{\theta}_U = 0.5$ when $f = f_{1/2}$. Based on reasonable expectations for the force-free equilibrium constant for native-to-denatured spectrin, it seems reasonable to assume that $f_{1/2} \sim$ 1-10 pN. Substitution yields the fraction of unfolded repeats under an imposed force f:

$$\tilde{\theta}_U = \frac{\exp[(f - f_{1/2})\Delta\Delta x/k_BT]}{1 + \exp[(f - f_{1/2})\Delta\Delta x/k_BT]} \qquad \text{(A4.3)}$$

Coupling the model of unfoldable repeats to an elastic chain of such repeats, a spectrin strand is assumed to have a fixed total number of domains, $N = \tilde{F} + \tilde{U}$. The total end-to-end length of the strand, $\tilde{X}$, is then equated to the end-to-end length of folded repeats, having length $\tilde{x}_F$, plus the length, $\tilde{x}_U$, of unfolded repeats (i.e., $\tilde{X} = \tilde{F}\tilde{x}_F + \tilde{U}\tilde{x}_U$). The end-to-end length scaled by the folded length is thus:

$$\tilde{X}/NL_F = \frac{\tilde{F}}{N}\frac{\tilde{x}_F}{L_F} + \frac{\tilde{U}}{N}\frac{\tilde{x}_U}{L_U}\frac{L_U}{L_F} \qquad \text{(A4.4)}$$

where L_U and L_F are the contour lengths of unfolded and folded repeats, respectively. Since $\tilde{F}/N$ and $\tilde{U}/N$ are, respectively, the fractions of folded and unfolded repeats,

$$\tilde{X}/NL_F = (1 - \tilde{\theta}_U)\frac{\tilde{x}_F}{L_F} + \tilde{\theta}_U\frac{\tilde{x}_U}{L_U}\frac{L_U}{L_F} \qquad \text{(A4.5)}$$

For analytic simplicity, $\tilde{x}_F/L_F$ and $\tilde{x}_U/L_U$ are both estimated by assuming a freely jointed chain in series:

$$\frac{\tilde{x}}{L} = \coth\left(\frac{2f\cdot p}{k_BT}\right) - \frac{k_BT}{2f\cdot p} \qquad \text{(A4.6)}$$

where p is a suitable persistence length. For a folded spectrin strand, p ought to approximate the length of a folded repeat, and so we assume p_F = 2.5 nm for folded spectrin even though it ought to be longer. For an unfolded spectrin domain, the persistence length is assumed to be a titin-like p_u = 0.5 nm (Rief et al., 1997). The ratio L_U/L_F is very reasonably taken to be ~9.25.

Substituting Eqs. A4.3 and A4.6 into Eq. A4.5 yields a relationship between the relative extensional force, $f/f_{1/2}$, and the relative unfolded length, $\tilde{X}/NL_F$, that is readily plotted with given parameters (Fig. 12). As the extensional force increases, this single spectrin strand initially exhibits classical strain-stiffening, where the effective spring constant ($k_{SP} \sim df/d\tilde{X}$) increases with extension (Fig. 12, *inset*). However, as the imposed extensional force approaches $f_{1/2}$, the spring constant decreases due to the unfolding of repeats (Fig. 12, *inset*). This single chain-softening qualitatively resembles the results for the network in which the force versus extension curve displays a decreasing slope (Fig. 10, *inset*).

One clear difference between the above single-molecule, two-state model and experimental results for the spectrin-actin network is that the spring constant *strictly* decreases with increasing axial extension of the network from the projection's tip to its pipette-constrained base (Fig. 8 *C*). No evidence of the present two-state model's strain-stiffening is obvious in experiment. Importantly, however, collective mechanical responses in large deformation are not strictly reflective of elemental responses. For instance, when tied together in a perfect triangulated lattice and then stressed, even the simplest Hookean spring—where the force is proportional to a change in length—exhibits highly nonlinear behavior, including phase transitions (Discher et al., 1997). Conversely, Monte Carlo simulations of cell-shaped networks (Fig. 7 *A*) show that a collection of strain-stiffening worm-like chains in aspiration collectively exhibit very little to no local stiffening as a fluctuating network (Discher et al., 1998). Unfolding of spectrin repeats could also be part of a more complex response: unfolding could lead to enhanced rotational motions of F-actin protofilaments that are already known to exhibit randomized azimuthal orientation in network deformation (Picart et al., 2000).

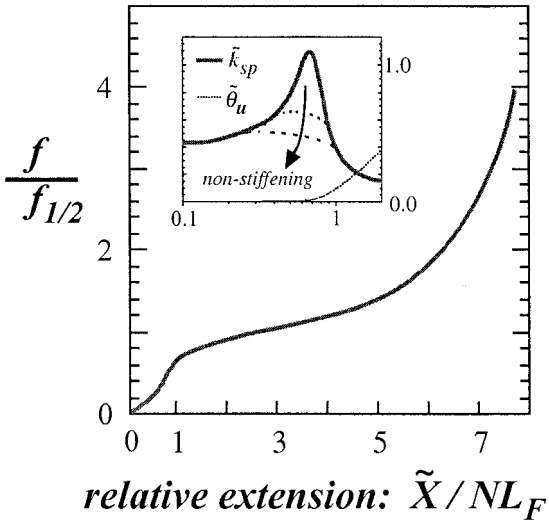

FIGURE 12 1D, two-state model for the extension and unfolding of spectrin. The relative extensional force versus the relative unfolded length, $\tilde{L}/Nl_F$, where the latter was calculated for different relative extension forces, f/f_d. (*Inset*) The effective spring constant is calculated from the numerical derivative, $\tilde{k}_{sp} = [d(f/f_d)/d(\tilde{L}/Nl_F)]$, and clearly depends on chain length. A softer spring is obtained when $f/f_d \geq 1$, whereupon a small but significant fraction, $\tilde{\theta}_u$, of spectrin repeats unfold. The additional dashed lines schematically denoted for a "non-stiffening" chain indicate suppression of the nonlinear stiffening response through, for example, partial unfolding.

We are grateful to Prof. David Meaney for the generous loan of the intensified CCD camera. We also thank Dr. Ranjan Mukhopadhyay (Penn Physics) for a careful reading of the revised manuscript, Prof. Tom Lubensky for many helpful discussions, and Prof. Evan Evans for suggesting a careful look at fluctuation frequencies.

This work was supported by a National Institutes of Health R01 grant and a Whitaker Foundation grant (to D.D.).

REFERENCES

Ahsan, A., J. Rudnick, and R. Bruinsma. 1998. Elasticity theory of the B-DNA to S-DNA transition. *Biophys. J.* 74:132–137.

Boey, S. K., D. H. Boal, and D. E. Discher. 1998. Simulations of the erythrocyte cytoskeleton at large deformation. I. Microscopic models. *Biophys. J.* 75:1573–1583.

Byers, T. J., and D. Branton. 1985. Visualization of the protein associations in the erythrocyte membrane skeleton. *P.N.A.S.* 82:6153–6157.

Carl, P., C. H. Kwok, G. Manderson, D. W. Speicher, and D. E. Discher. 2001. Forced unfolding modulated by disulfide bonds in the Ig domains of a cell adhesion molecule. *Proc. Nat. Acad. Sci. U.S.A.* 98:1565–1570.

Carrion-Vazquez, M., P. E. Marszalek, A. F. Oberhauser, J. M. Fernandez. 1999. Atomic force microscopy captures length phenotypes in single proteins. *Proc. Nat. Acad. Sci. USA.* 96:11288–11292.

Chaikin, P. M., and T. C. Lubensky. 1995. Principles of Condensed Matter Physics. Cambridge University Press.

Chasis, J. A., and N. Mohandas. 1992. Red blood cell glycophorins. *Blood.* 80:1869–1879.

DeSilva, T. M., K. C. Peng, K. D. Speicher, and D. W. Speicher. 1992. Analysis of human red cell spectrin tetramer (head-to-head) assembly using complementary univalent peptides. *Biochemistry*. 31: 10872–10878.

Discher, D. E., D. H. Boal, and S. K. Boey. 1997. Phase transitions and anisotropic responses of planar triangular nets under large deformation. *Phys. Rev. E.* 55:4762–4772.

Discher, D. E., D. H. Boal, and S. K. Boey. 1998. Simulations of the erythrocyte cytoskeleton at large deformation. II. Micropipette aspiration. *Biophys. J.* 75:1584–1597.

Discher, D. E., and N. Mohandas. 1996. Kinematics of red cell aspiration by fluorescence-imaged microdeformation. *Biophys. J.* 71:1680–1694.

Discher, D. E., N. Mohandas, and E. A. Evans. 1994. Molecular maps of red cell deformation: hidden elasticity and in situ elasticity. *Science.* 266:1032–1035.

Discher, D. E., R. Winardi, P. O. Schischmanoff, M. Parra, J. G. Conboy, and N. Mohandas. 1995. Mechanochemistry of protein 4.1's spectin-actin binding domain: ternary complex interactions, membrane binding, network integration, structural strengthening. *J. Cell Biol.* 130:897–907.

Evans, E. A. 1973. A new material concept for the red cell membrane. *Biophys. J.* 13:926–940.

Evans, E. A., and R. Skalak. 1980. Mechanics and Thermodynamics of Biomembranes. CRC Press, Boca Raton, FL.

Evans, E., N. Mohandas, and A. Leung. 1984. Static and dynamic rigidities of normal and sickle erythrocytes. Major influence of cell hemoglobin concentration. *J. Clin. Invest.* 73:477–488.

Evans, E., and W. Rawicz. 1990. Entropy-driven tension and bending elasticity in condensed-fluid membranes. *Phys. Rev. Lett.* 64:2094.

Evans, E., and K. Ritchie. 1999. Strength of a weak bond connecting flexible polymer chains. *Biophys. J.* 76:2439–2447.

Evans, E., A. Leung, D. Hammer, and S. Simon. 2001. Chemically distinct transition states govern rapid dissociation of single L-selectin bonds under force. *P.N.A.S.* 98:3784–3789.

Feng, S., and P. N. Sen. 1984. Percolation on elastic networks: new exponent and threshold. *Phys. Rev. Lett.* 52:216–219.

Gittes, F., B. Schnurr, P. D. Olmsted, F. C. MacKintosh, and C. F. Schmidt. 1997. Microscopic viscoelasticity: shear moduli of soft materials determined from thermal fluctuations. *Phys. Rev. Lett.* 79:3286–3289.

Golan, D. E., and W. Veatch. 1980. Lateral mobility of band 3 in the human erythrocyte membrane studied by fluorescence photobleaching recovery: evidence for control by cytoskeletal interactions. *Proc. Natl. Acad. Sci. U.S.A.* 77:2537–2541.

Hansen, J. C., R. Skalak, S. Chien, and A. Hoger. 1997. Influence of network topology on the elasticity of the red blood cell membrane skeleton. *Biophys. J.* 72:2369–2381.

Helfer, E., S. Harlepp, L. Bourdieu, J. Robert, F. C. MacKintosh, and D. Chatenay. 2000. Microrheology of biopolymer-membrane complexes. *Phys. Rev. Lett.* 85:457–460.

Hénon, S., G. Lenormand, A. Richert, and F. Gallet. 1999. A new determination of the shear modulus of the human erythrocyte membrane using optical tweezers. *Biophys. J.* 76:1145–1151.

Hicks, B. W., and K. J. Angelides. 1995. Tracking movements of lipids and thyl molecules in the plasmalemma of living fibroblasts by fluorescence video microscopy with nanometer scale precision. *J. Membr. Biol.* 144:231–244.

Hill, T. L. 1985. Cooperativity Theory in Biochemistry: Steady-State and Equilibrium Systems. Springer-Verlag, New York.

Hochmuth, R. M., and R. E. Waugh. 1987. Erythrocyte membrane elasticity and viscosity. *Annu. Rev. Physiol.* 49:209–219.

Landau, L. D., and E. M. Lifshitz. 1959. Theory of Elasticity. Pergamon Press, London.

Lee, J. C-M., D. T. Wong, and D. E. Discher. 1999. Direct measures of large, anisotropic strains in deformation of the erythrocyte cytoskeleton. *Biophys. J.* 77:853–864.

Lenne, P. F., A. J. Raae, S. M. Altmann, M. Saraste, and J. K. Horber. 2000. States and transitions during forced unfolding of a single spectrin repeat. *FEBS Lett.* 476:124–128.

Lieber, M. R., and T. L. Steck. 1989. Hemolytic holes in human erythrocyte membrane ghosts. *Methods. Enzymol.* 173:356–367.

Liphardt, J., B. Onoa, S. B. Smith, I. Tinoco, Jr., and C. Bustamante. 2001. Reversible unfolding of single RNA molecules by mechanical force. *Science.* 292:733–737.

Markle, D. R., E. A. Evans, and R. M. Hochmuth. 1983. Force relaxation and permanent deformation of erythrocyte membrane. *Biophys. J.* 42: 91–98.

McGrath, J. L., J. H. Hartwig, and S. C. Kuo. 2000. The mechanics of F-actin microenvironments depend on the chemistry of probing surfaces. *Biophys. J.* 79:3258–3266.

Mohandas, N., and E. A. Evans. 1994. Mechanical properties of the red cell membrane in relation to molecular structure and genetic defects. *Annu. Rev. Biophys. Biomol. Struct.* 23:787–818.

Ohanian, V., L. C. Wolfe, K. M. John, J. C. Pinder, S. E. Lux, and W. B. Gratzer. 1984. Analysis of the ternary interaction of the red cell membrane skeletal proteins spectrin, actin, and 4.1. *Biochemistry*. 23: 4416–4420.

Picart, C., P. Dalhaimer, and D. E. Discher. 2000. Actin protofilament orientation in deformation of the erythrocyte membrane skeleton. *Biophys. J.* 79:2987–3000.

Picart, C., and D. E. Discher. 1999. Actin protofilament orientation at the erythrocyte membrane. *Biophys. J.* 77:856–878.

Rief, M., J. M. Fernandez, and H. E. Gaub. 1998. Elastically coupled two-level systems as a model for biopolymer extensibility. *Phys. Rev. Lett.* 81:4764–4767.

Rief, M., M. Gautel, F. Oesterhelt, J. M. Fernandez, and H. E. Gaub. 1997. Reversible unfolding of individual titin immunoglobulin domains by AFM. *Science.* 276:1109–1112.

Rief, M., J. Pascual, M. Saraste, and H. E. Gaub. 1999. Single molecule force spectroscopy of spectrin repeats: low unfolding forces in helix bundles. *J. Mol. Biol.* 286:553–561.

Sheetz, M. P., S. Turney, H. Qian, and E. L. Elson. 1989. Nanometer-level analysis demonstrates that lipid flow does not drive membrane glycoprotein movements. *Nature.* 340:284–288.

Shen, B. W., R. Josephs, and T. L. Steck. 1986. Ultrastructure of the intact skeleton of the human erythrocyte membrane. *J. Cell Biol.* 102: 997–1006.

Simson, D. A., F. Ziemann, M. Strigl, and R. Merkel. 1998. Micropipette-based pico force transducer: in-depth analysis and experimental verification. *Biophys. J.* 74:2080–2088.

Strey, H., M. Peterson, and E. Sackmann. 1995. Measurement of erythrocyte membrane elasticity by flicker eigenmode decomposition. *Biophys. J.* 69:478–488.

Stokke, B. T., A. Mikkelson, and A. Elgsaeter. 1986. The human erythrocyte membrane may be an ionic gel. I. Membrane mechanochemical properties. *Eur. Biophys. J.* 13:203–218.

Takakuwa, Y., G. Tchernia, M. Rossi, M. Benabadji, and N. Mohandas. 1986. Restoration of normal membrane stability to unstable protein 4.1-deficient erythrocyte membranes by incorporation of purified protein 4.1. *J. Clin. Invest.* 78:80–85.

Takeuchi, M., H. Miyamoto, Y. Sako, H. Komizu, and A. Kusumi. 1998. Structure of the erythrocyte membrane skeleton as observed by atomic force microscopy. *Biophys. J.* 74:2171–2183.

Tolomeo, J. A., C. R. Steele, and M. C. Holley. 1996. Mechanical properties of the lateral cortex of mammalian auditory outer hair cells. *Biophys. J.* 71:421–429.

Tomishige, M., and A. Kusumi. 1999. Compartmentalization of the erythrocyte membrane by the membrane skeleton: intercompartmental hop diffusion of band 3. *Mol. Biol. Cell.* 10:2475–2479.

Ursitti, J. A., and V. M. Fowler. 1994. Immunolocalization of tropomodulin, tropomyosin and actin in spread human erythrocyte skeletons. *J. Cell Sci.* 107:1633–1639.

Waugh, R. E., and P. Agre. 1988. Reductions of erythrocyte membrane viscoelastic coefficients reflect spectrin deficiencies in hereditary spherocytosis. *J. Clin. Invest.* 81:133–141.

Waugh, R., and E. A. Evans. 1979. Thermoelasticity of red blood cell membrane. *Biophys. J.* 26:115–131.

Yamada, S., D. Wirtz, and S. C. Kuo. 2000. Mechanics of living cells measured by laser tracking microrheology. *Biophys. J.* 78:1736–1747.